energies

MDPI

Article

DC Side Bus Voltage Control of Wind Power Grid-Connected Inverter Based on Second-Order Linear Active Disturbance Rejection Control

Youjie Ma [1,2], Faqing Zhao [1,2,*], Xuesong Zhou [1,2], Mao Liu [1,2] and Bao Yang [1,2]

[1] Tianjin Key Laboratory for Control Theory and Application in Complicated Systems, Tianjin University of Technology, Tianjin 300384, China; sjteam2016@126.com (Y.M.); zxsmyj@126.com (X.Z.); mao_tjlg@163.com (M.L.); tjutsjteam@163.com (B.Y.)

[2] School of Electrical and Electronic Engineering, Tianjin University of Technology, Tianjin 300384, China

* Correspondence: zhaofaqingcx@163.com; Tel.: +86-152-2237-4569

Received: 16 October 2019; Accepted: 7 November 2019; Published: 9 November 2019

Abstract: In order to improve the dynamic response speed and the steady-state performance of the DC side bus voltage of the wind power grid-connected inverter, a mathematical model of a typical three-phase voltage type PWM (Pulse Width Modulation, PWM) grid-connected inverter was established, and its traditional voltage-current double closed loop with proportional-integral control method was analyzed. Then a second-order linear active disturbance rejection controller that does not depend on system model information was designed to replace the traditional voltage outer loop proportional-integral controller, thus a new double closed-loop control structure was formed to control it. The frequency domain theory was used to analyze the convergence of the third-order linear extended state observer and the influence of the total disturbance on the performance of the third-order linear extended state observer. The parameter tuning scheme of the designed controller was given. Finally, the 1.5 MW direct-driven permanent magnet wind power generation system was built in the Matlab/Simulink software and the control effects of the two control modes under different working conditions are compared. The simulation results show that the control scheme designed in this paper is superior to the traditional proportional-integral controller which has good anti-interference characteristics and robustness. Especially it has a good stability effect on DC side bus voltage fluctuations.

Keywords: wind power grid-connected inverter; dual-loop control; second-order linear active disturbance rejection; linear extended state observer; frequency domain analysis

1. Introduction

In recent years, with the continuous improvement of installed capacity of wind power generation systems, the grid-connected inverter—as an interface device directly connected with the power grid in wind power generation systems which controls performance—will directly affect the quality of output power and the operating efficiency of the system [1,2]. For the control system of direct-driven permanent magnet wind power, the grid-connected inverter is not only necessary to realize the maximum power factor grid-connected and control the grid-connected current, but also to control the DC side bus voltage in a reasonable range [3]. As the intermediate link of energy transmission and conversion in wind power systems, the stability of DC side voltage not only directly influences whether independent control of the converter on the machine side and the converter on the grid side can be achieved but also whether the system can be operated in a safe and stable state. Therefore, the design of the grid-connected inverter control system is the core of the entire wind power system control [4].

For the control of the DC side bus voltage of the wind power grid-connected inverter, traditional method generally adopts the double closed loop structure of the voltage outer loop and the current inner loop based on the grid voltage vector orientation [5]. In this structure, the outer loop controls the voltage of the bus capacitor terminal through a proportional-integral (PI) controller, and the inner loop is used to track the output command of the outer loop. The inner loop also generally adopts a PI controller. The direct current signal provided by the inner loop controller is converted into an alternating current signal in stationary coordinates by coordinate transformation, and the signal is used as a pulse-triggered modulation signal, thereby realizing control of the DC side bus voltage. Although the traditional voltage-current double-closed-loop with PI control method has been widely applied in practical engineering and has achieved certain effects, with the development of modern control technology and the more stringent grid-connected requirements under the new form, the drawbacks of traditional PI control methods in engineering applications are increasingly apparent. This passive control method based on error to eliminate the error has a certain hysteresis compared with the influence of the disturbance, and may also cause the system to generate oscillation or large overshoot due to the excessively applied control force. Although the addition of integrals can eliminate the error of the system, it also brings problems such as phase angle lag, and the ability of the controller to suppress changes and unknown disturbances is not obvious [6].

In order to improve the shortcomings of the traditional control methods and improve the control performance of the DC side bus voltage, in [7], in view of the traditional double-closed-loop PI control method of wind power grid-connected inverters, the sliding-film algorithm and the traditional PI controller are combined to regulate the grid-side converter. Compared with the traditional control method, this method has improved the sinusoidal saturation of grid-connected current and the anti-disturbance performance of DC side bus voltage. However, the parameter adjustment of the controller is complex which is not conducive to engineering application. In [8], the synovial variable structure control is used in the voltage outer loop, and the inner loop is used for the predictive current control which effectively suppresses the grid side current harmonics and making the DC side voltage more stable. Liao et al. [2] take the DC bus voltage of the grid-connected inverter of the photovoltaic power generation system as control object. A direct power control method based on non-linear disturbance observer is proposed to deal with the large fluctuation of DC bus voltage when the output power of photovoltaic panels suddenly changes. Without adding additional sensors, the output power of photovoltaic panel is observed in real time by using disturbance observer, and the observation value is added as feed-forward into the power inner loop, so that the power inner loop is given to contain input power information so as to improve the control performance of DC bus voltage. In [9], a new control strategy is proposed for the permanent magnet synchronous generator grid-connected inverter system. For the grid-side, a novel controller is proposed for the first time to be successfully used for the direct-drive wind energy conversion system, combining a proportional complex integral current inner loop based on stationary reference frame for regulating the grid-side current with a DC voltage outer loop for stabilizing the DC bus voltage. However, the controller parameters are complicated to adjust, which is not conducive to engineering applications.

The above research aimed to achieve the precise control of the DC side bus voltage by improving the traditional PI controller or introducing more advanced controller to replace it. However, all of the above studies need to be based on a more accurate system model to design the controller, which brings great challenges undoubtedly. The wind power grid-connected inverter, as a complex system with non-linearity, multi-variable coupling and vulnerable to grid voltage fluctuations and load changes, is difficult to establish an accurate mathematical model for, which is also one of the reasons for the unsatisfactory results of traditional control schemes. Active Disturbance Rejection Control (ADRC) [10,11] is derived from the advantages of traditional PID (Proportion Integration Differentiation, PID) control technology after rethinking modern control theory. The design of the controller does not depend on the mathematical model of the system, and uses its own Extended State Observer (ESO) to observe and compensate the internal and external disturbances of the system so that

the disadvantages of the traditional PI controller can be well solved. In [12], a control strategy based on second-order ADRC is proposed for the wind power generation system fault crossing of doubly fed induction generator. The integrated design of flux damping method is adopted in this control strategy, which improves the robustness and effectiveness of flux damping method under complex working conditions. In [13], for the influence of periodic interference sources on wind turbines, a pitch control scheme based on auto-disturbance rejection control is proposed. The simulation results of the proposed control scheme show an improved load reduction compared to other control techniques by realistic simulations of several different wind speeds and average wind speeds. In [14], the ADRC of reduced-order extended state observer is introduced into the LCL high-order filter of grid-connected inverters, which compensates the resonant poles of the LCL filter by canceling the zero-pole. This method is still valid under the case of uncertainties of grid impedance and filter parameters, and does not require control tuning. In [15], the idea of ADRC is applied to the grid-connected control of the micro-grid, and a second-order nonlinear ADRC operation controller is designed to make the micro-grid operate stably and smoothly under the switching between grid-connected and isolated islands and load disturbance. The second-order nonlinear ADRC operation controller with stable and smooth cooperation between the grids has better control effect than the traditional PI controller. However, the parameter adjustment of nonlinear ADRC is more complicated.

In view of the fact that the difficulty of traditional nonlinear ADRC parameter adjustment hinders its wide application in engineering, the controller was linearized and parameterized in previous studies [16,17], which promotes the application of ADRC in engineering [18–21]. In this paper, the direct-driven permanent magnet wind power grid-connected inverter is taken as the research object. Based on the analysis of its traditional control method, the second-order Linear Active Disturbance Rejection Control (LADRC) is designed as its voltage outer loop controller, and the current inner loop still uses PI controller. Accurate control of DC side bus voltage in various disturbances is realized without adding additional disturbance observation sensors. The classical control theory is used to analyze the convergence of the third-order linear extended state observer and the influence of the total disturbance on the performance of the third-order linear extended state observer in the frequency domain. Finally, the effectiveness of the control strategy designed in this paper is verified by comparative simulation experiments.

2. Mathematical Model and Traditional Control Strategy of Wind Power Grid-Connected Inverter

2.1. Mathematical Model of Wind Power Grid-Connected Inverter

The circuit topology of the classic three-phase voltage-type PWM wind power grid-connected inverter is shown in Figure 1. Its main control objective is to achieve the power balance of the system, stabilize the DC side bus voltage and generate AC current that meets the grid-connected conditions.

The DC side is replaced by a capacitor in the structure diagram and the grid is replaced by three-phase voltage sources, where U_{dc} is DC side bus voltage. L is grid-side filter inductor. R is the equivalent resistance. i_a, i_b and i_c are grid-side converter output phase current. i_{ao}, i_{bo} and i_{co} are current flowing into the grid. e_a, e_b and e_c are power voltage. u_a,u_b and u_c are phase voltage of the grid side inverter output. i_{dc} is current flowing into the grid-connected inverter and i_L is current flowing into the grid. By defining the switch function $S_k(k = a, b, c)$. When $S_k = 1$ which means the upper arm of the inverter is conducting. When $S_k = 0$, this means the lower arm of the inverter is conducting. Under the voltage and current reference directions shown in Figure 1 and according to Kirchhoff's voltage rule, the mathematical model of the three-phase stationary coordinate system based on the switching function of the grid-connected inverter is Equation (1) [22,23]:

$$\begin{cases} \mathrm{L}\frac{di_\mathrm{a}}{dt} = -\mathrm{R}i_\mathrm{a} - e_\mathrm{a} + \left(S_\mathrm{a} - \frac{S_\mathrm{a}+S_\mathrm{b}+S_\mathrm{c}}{3}\right)U_\mathrm{dc} \\ \mathrm{L}\frac{di_\mathrm{b}}{dt} = -\mathrm{R}i_\mathrm{b} - e_\mathrm{b} + \left(S_\mathrm{b} - \frac{S_\mathrm{a}+S_\mathrm{b}+S_\mathrm{c}}{3}\right)U_\mathrm{dc} \\ \mathrm{L}\frac{di_\mathrm{c}}{dt} = -\mathrm{R}i_\mathrm{c} - e_\mathrm{c} + \left(S_\mathrm{c} - \frac{S_\mathrm{a}+S_\mathrm{b}+S_\mathrm{c}}{3}\right)U_\mathrm{dc} \\ \mathrm{C}\frac{dU_\mathrm{dc}}{dt} = -S_\mathrm{a}i_\mathrm{a} - S_\mathrm{b}i_\mathrm{b} - S_\mathrm{c}i_\mathrm{c} + i_\mathrm{dc} \end{cases} \tag{1}$$

The equation of state for converting Equation (1) to Equation (2) is:

$$\frac{d}{dt}\begin{bmatrix} i_\mathrm{a} \\ i_\mathrm{b} \\ i_\mathrm{c} \end{bmatrix} = \begin{bmatrix} -\frac{\mathrm{R}}{\mathrm{L}} & 0 & 0 \\ 0 & -\frac{\mathrm{R}}{\mathrm{L}} & 0 \\ 0 & 0 & -\frac{\mathrm{R}}{\mathrm{L}} \end{bmatrix}\begin{bmatrix} i_\mathrm{a} \\ i_\mathrm{b} \\ i_\mathrm{c} \end{bmatrix} + \begin{bmatrix} \frac{U_\mathrm{dc}}{\mathrm{L}}\left(S_\mathrm{a} - \frac{S_\mathrm{a}+S_\mathrm{b}+S_\mathrm{c}}{3}\right) - \frac{e_\mathrm{a}}{\mathrm{L}} \\ \frac{U_\mathrm{dc}}{\mathrm{L}}\left(S_\mathrm{b} - \frac{S_\mathrm{a}+S_\mathrm{b}+S_\mathrm{c}}{3}\right) - \frac{e_\mathrm{b}}{\mathrm{L}} \\ \frac{U_\mathrm{dc}}{\mathrm{L}}\left(S_\mathrm{c} - \frac{S_\mathrm{a}+S_\mathrm{b}+S_\mathrm{c}}{3}\right) - \frac{e_\mathrm{c}}{\mathrm{L}} \end{bmatrix} \tag{2}$$

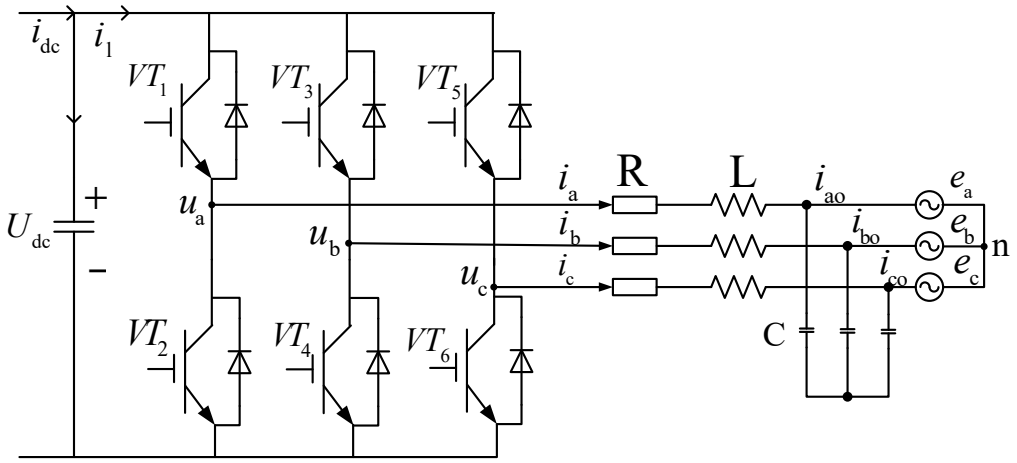

Figure 1. Circuit topology of three-phase voltage type PWM wind power grid-connected inverter.

It can be seen from the equation of state that the voltages of the phases of the inverter output can be changed by controlling the switching state of the inverter, thereby changing the current and realizing the output of electric energy from the inverter to the grid. However, the mathematical model of the grid-side inverter in the three-phase static coordinate system contains varying AC quantities, which hinders the controller of our design system. So, it is necessary to convert the mathematical model under the three-phase static coordinate system to the two-phase synchronous rotating coordinate system. In the two-phase synchronous rotating coordinate system that the time-varying alternating current is converted into a direct current amount and thereby simplifying the control system design. The equation of state of the system in two-phase synchronous rotating d-q coordinate system can be obtained as Equation (3) after coordinate transformation:

$$\begin{bmatrix} \frac{di_\mathrm{d}}{dt} \\ \frac{di_\mathrm{q}}{dt} \end{bmatrix} = \begin{bmatrix} -\frac{\mathrm{R}}{\mathrm{L}} & \omega \\ -\omega & -\frac{\mathrm{R}}{\mathrm{L}} \end{bmatrix}\begin{bmatrix} i_\mathrm{d} \\ i_\mathrm{q} \end{bmatrix} + \begin{bmatrix} \frac{1}{\mathrm{L}}(S_\mathrm{d}\cdot U_\mathrm{dc} - e_\mathrm{d}) \\ \frac{1}{\mathrm{L}}\left(S_\mathrm{q}\cdot U_\mathrm{dc} - e_\mathrm{q}\right) \end{bmatrix} \tag{3}$$

where ω is synchronous electrical angular velocity. e_d and e_q are the d, q axis component of the grid voltage. i_d and i_q are the d, q-axis component of the alternating current on the grid side. S_d and S_q are the switching function for the d, q axis.

The output voltage of the wind power grid-connected inverter switch has the following formula:

$$\begin{cases} U_\mathrm{d} = S_\mathrm{d}U_\mathrm{dc} \\ U_\mathrm{q} = S_\mathrm{q}U_\mathrm{dc} \end{cases} \tag{4}$$

Therefore, the mathematical model of the wind power grid-connected inverter obtained by Equation (3) and Equation (4) under the two-phase synchronous rotating d-q coordinate system is Equation (5):

$$\begin{cases} U_{\mathrm{d}} = e_{\mathrm{d}} - \mathrm{R}i_{\mathrm{d}} - \mathrm{L}\frac{di_{\mathrm{d}}}{dt} + \omega \mathrm{L}i_{\mathrm{q}} \\ U_{\mathrm{q}} = e_{\mathrm{q}} - \mathrm{R}i_{\mathrm{q}} - \mathrm{L}\frac{di_{\mathrm{q}}}{dt} - \omega \mathrm{L}i_{\mathrm{d}} \end{cases} \tag{5}$$

It can be seen from the above equation that the AC quantity in the mathematical model of three-phase static ABC coordinate system is converted to DC quantity in two-phase rotating d-q coordinate system after coordinate transformation, which simplifies the established mathematical model of the system and makes the design of the system controller more convenient.

2.2. Voltage and Current Double Closed Loop PI Control Strategy Analysis

The traditional control method of wind power grid-connected inverter is to adopt voltage external loop and current inner loop double PI control structure based on grid voltage vector orientation. The DC side bus voltage can be kept stable in this control mode and the AC side can output a good sinusoidal current waveform so that the inverter reaches the maximum power factor grid connection requirement. The control of the voltage outer loop is adjusted based on the difference between the given and feedback of the DC side voltage, thereby achieving the purpose of maintaining voltage stability. The output of the external loop is the given value of the d-axis current of the inner loop, and the main purpose of the current inner loop is to achieve fast tracking of the given.

In the coordinate transformation process, the d-axis direction is aligned with the grid voltage space vector **E**, that is, the peak point of the grid voltage a phase is taken as the zero point of the rotation angle θ, while $e_{\mathrm{d}} = |\mathbf{E}|$, $e_{\mathrm{q}} = 0$. The vector diagram of the transformation between $\alpha - \beta$ and d-q coordinates is shown in Figure 2.

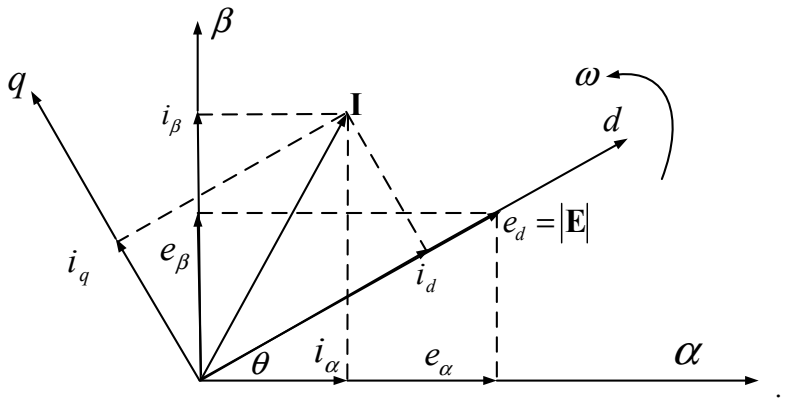

Figure 2. Grid-connected inverter voltage and current vector diagram under $\alpha - \beta$ and d–q coordinates.

In Figure 2, i_{d} and i_{q} are the active and reactive components in the grid side current. u_{d} and u_{q} are the output control quantities. In steady state, since i_{d} and i_{q} are both direct current and their differential term is equal to zero, the steady-state Equation (6) is obtained according to Equation (5):

$$\begin{cases} U_{\mathrm{d}} = e_{\mathrm{d}} - \mathrm{R}i_{\mathrm{d}} + \omega \mathrm{L}i_{\mathrm{q}} \\ U_{\mathrm{q}} = -\mathrm{R}i_{\mathrm{q}} - \omega \mathrm{L}i_{\mathrm{d}} \end{cases} \tag{6}$$

According to Equation (6), the steady-state voltage vector diagram of the grid-connected inverter can be obtained as shown in Figure 3:

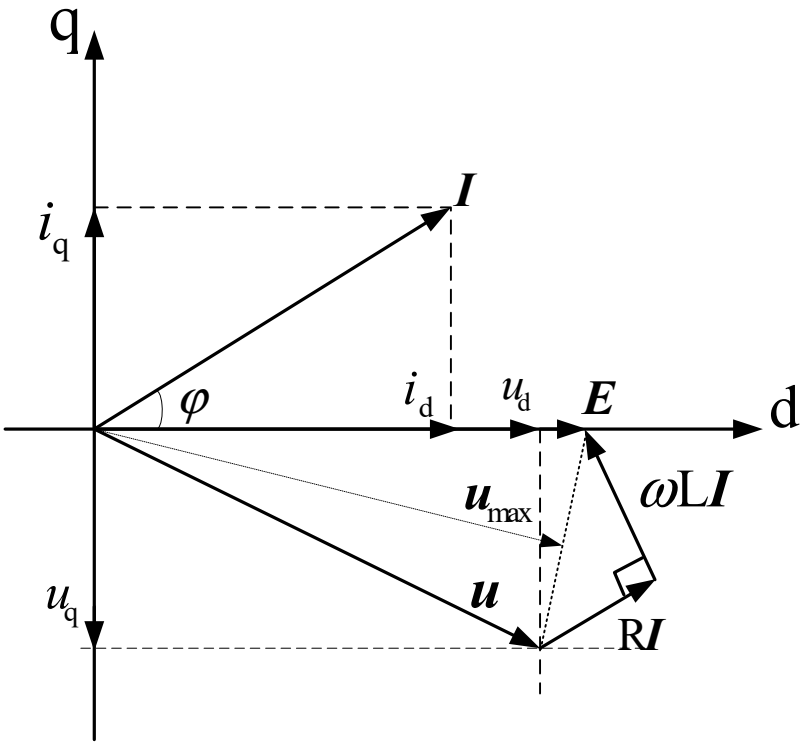

Figure 3. Steady-state voltage space vector diagram of grid-side inverter.

In Figure 3, φ is the power factor angle, $\boldsymbol{E}$ and $\boldsymbol{I}$ are the grid voltage and current vectors and $\boldsymbol{u}$ is the AC side voltage vector of the grid side converter.

In Equation (6), e_d is the feed-forward component of grid voltage which can overcome the disturbance caused by grid voltage fluctuation. $\omega L i_d$ and $\omega L i_q$ are decoupled terms so that the active and reactive currents can be controlled separately. In the double closed-loop structure, in order to maintain the stability of the DC side bus voltage, the output of the voltage outer loop is taken as the given value of the active current in the current inner loop and the reactive current is given by the outside. In order to realize grid connection of unit power factor, the given value of reactive current is set to zero. After the active and reactive currents are fed back by the inner current loop, the closed-loop output is superimposed into the steady-state control equation, and the control quantities u_d and u_q can be output. The control block diagram of three-phase voltage type PWM grid-connected inverter under the traditional control mode is shown in Figure 4.

Set k_{up} and k_{ui} to be the proportional and integral coefficients of the voltage outer loop controller respectively, k_{ip} and k_{ii} to be respectively the proportional and integral coefficient of the current inner loop controller, and the final grid-connected inverter control model can be obtained as Equation (7):

$$\begin{cases} i^*_d = k_{up}(U^*_{dc} - U_{dc}) + k_{ui}\int (U^*_{dc} - U_{dc})dt \\ i^*_q = 0 \\ u_d = e_d - Ri_d + \omega L i_d - k_{ip}(i^*_d - i_d) - k_{ii}\int (i^*_d - i_d)dt \\ u_q = -Ri_q - \omega L i_d - k_{ip}\left(i^*_q - i_q\right) - k_{ii}\int \left(i^*_q - i_q\right)dt \end{cases} \tag{7}$$

where i^*_d and i^*_q are the given values of the inner loop d and q axes respectively. U^*_{dc} is the given value of the DC side bus voltage. Substituting Equation (5) into the above equation gives Equation (8):

$$\begin{cases} L\frac{di_d}{dt} = k_{ip}(i^*_d - i_d) + k_{ii}\int (i^*_d - i_d)dt \\ L\frac{di_q}{dt} = k_{ip}\left(i^*_q - i_q\right) + k_{ii}\int \left(i^*_q - i_q\right)dt \end{cases} \tag{8}$$

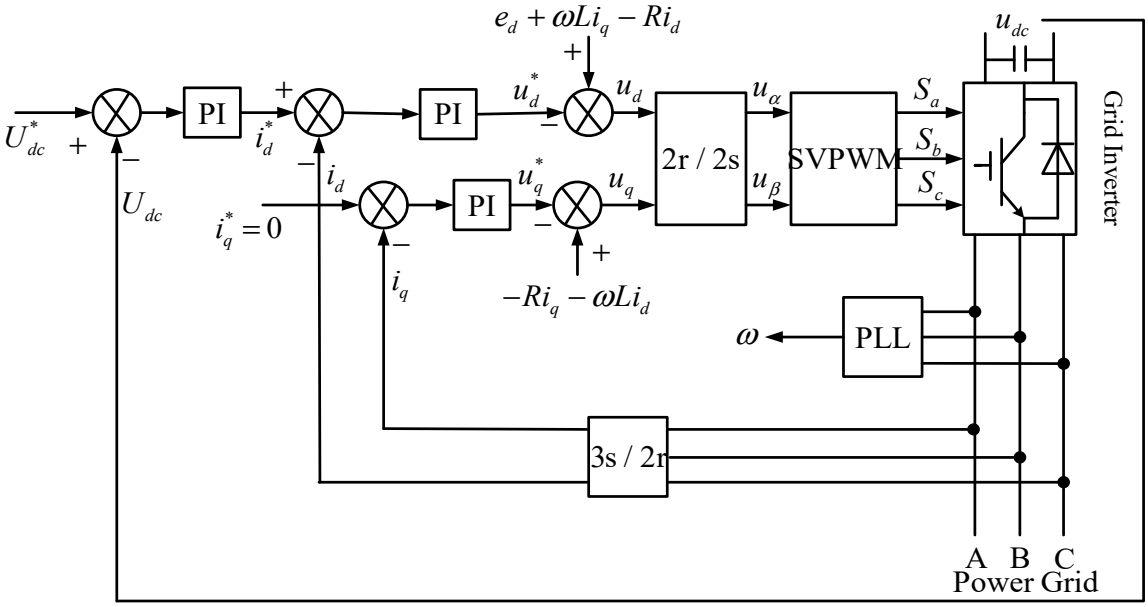

Figure 4. Control block diagram of grid-connected inverters under traditional control mode.

It can be seen from the above equation that both the control model of d-axis output current and the control model of q-axis output current on the grid side contain only their respective components so that the system achieves decoupling control [24]. In this way, it will be more accurate and simple when designing the PI controller of the system; thereby the control of the system becomes more precise. After designing the controller, the current inner loop controller parameters are selected according to the "first-order optimal" principle to obtain the optimal step response and the voltage outer loop controller parameters are set according to the "mode optimal" principle to get optimal regulation performance and ensure system stability [25]. It can be seen from Figure 4 that u_{d} and u_{q} are output as control variables. After coordinate transformation, the Space Vector Pulse Width Modulation (SVPWM) strategy interface will be connected, and the final switching function will be obtained to control the on and off of the grid-side inverter, thus realizing the control of the DC-side bus voltage.

3. The Principle of Second-Order LADRC

The second-order LADRC consists of a third-order Linear Extended State Observer (LESO), disturbance compensation and Linear State Error Feedback (LSEF).

3.1. Design of Third-Order LESO

The third-order LESO is the core of the second-order LADRC. It does not depend on the mathematical model of the system and can estimate the state variables of the controlled object and the real-time values of the generalized disturbances, and compensate them to simplify the controlled object [10,26]. A general second-order system expressed by a differential equation is shown in Equation (9):

$$\ddot{y} = -a_1 \dot{y} - a_2 y + b \cdot u + w \tag{9}$$

where y is the output of the system. u is the input of the system. w is the external disturbance. a_1 and a_2 are the system parameters. b is the control gain. a_1, a_2 and b are unknown and there is $b_0 \approx b$. Set $x_1 = y$, $x_2 = \dot{y}$ and $f = -a_1 \dot{y} - a_2 y + (b - b_0) \cdot u + w$, whose physical meaning is to contain the total

disturbance inside and outside the system and extending it to the new state variable $x_3 = f$ of the system. The equation of state of the system is given as Equation (10):

$$\begin{cases} \dot{x}_1 = x_2 \\ \dot{x}_2 = x_3 + b_0 u \\ \dot{x}_3 = h \\ y = x_1 \end{cases} \tag{10}$$

where x_1, x_2 and x_3 are the state variables of the system. $h = \dot{f}$.

Converting Equation (10) to the state space expression of Equation (11):

$$\begin{cases} \dot{x} = Ax + Bu + E\dot{f} \\ y = Cx \end{cases} \tag{11}$$

where:

$$A = \begin{bmatrix} 0 & 1 & 0 \\ 0 & 0 & 1 \\ 0 & 0 & 0 \end{bmatrix}, B = \begin{bmatrix} 0 \\ b_0 \\ 0 \end{bmatrix}, E = \begin{bmatrix} 0 \\ 0 \\ 1 \end{bmatrix}, C = \begin{bmatrix} 1 & 0 & 0 \end{bmatrix}.$$

The third-order LESO of the corresponding system is of Equation (12):

$$\begin{cases} \dot{z}_1 = z_2 - l_1(z_1 - y) \\ \dot{z}_2 = z_3 - l_2(z_1 - y) + b_0 u \\ \dot{z}_3 = -l_3(z_1 - y) \end{cases} \tag{12}$$

where l_1, l_2 and l_3 are the observer gains of the third-order LESO. Obviously, when we select the appropriate observer gains l_1, l_2 and l_3, the third-order LESO can estimate the all state variables of the original system, where z_1 is an estimated value of x_1, z_2 is an estimated value of x_2 and z_3 is an estimated value of x_3.

3.2. Disturbance Compensation Link

The traditional PI controllers eliminate the steady-state error of the system by integrating. However, the addition of the integral link tends to reduce the stability of the system and slow the dynamic response. The second-order LADRC can generate real-time estimates of generalized disturbances by means of third-order LESO and compensate the estimates to the system so that avoiding the side effects caused by the integral link. The control rate of the system is taken as Equation (13):

$$u = (-z_3 + u_0)/b_0 \tag{13}$$

where u_0 is the output of the linear error feedback control rate. Substituting the above formula into Equation (9) gives the following formula:

$$\ddot{y} = (f - z_3) + u_0 \approx u_0 \tag{14}$$

It can be seen from the above equation that when the estimation error of z_3 to f is neglected, that is $z_3 \approx f$, the system can become a double integral series structure which simplifies the control object and improves the control performance. That is the disturbance compensation.

3.3. Design of Linear State Error Feedback Control Rate

The nonlinear state error feedback control rate (nonlinear PD control) in ADRC becomes the linear state error feedback control rate (linear PD control) after being linearized. Then the output u_0 of the linear error feedback control rate as Equation (15):

$$u_0 = k_p(v - z_1) - k_d z_2 \tag{15}$$

where v is the given input of the controller. k_p and k_d are the controller parameters. According to Equations (14) and (15) that the closed-loop transfer function of the system can be obtained as Equation (16):

$$G(s) = \frac{k_p}{s^2 + k_d s + k_p} \tag{16}$$

The structure of the second-order LADRC can be obtained from the above analysis as shown in Figure 5:

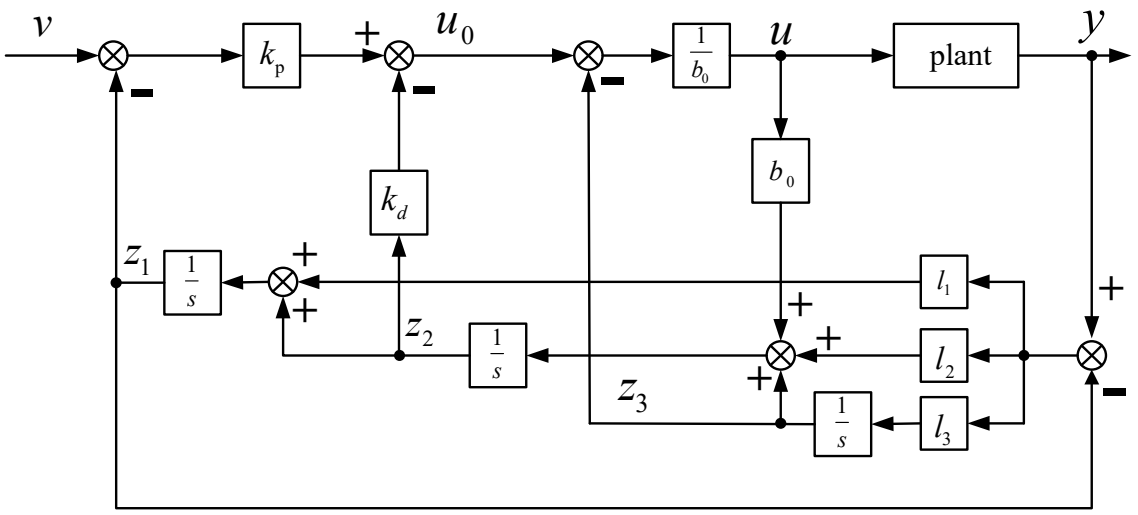

Figure 5. Second-order Linear Active Disturbance Rejection Control (LADRC) controller structure.

3.4. Parameters Tuning of Second-Order LADRC Controller

Whether the parameters setting of the third-order LESO and LSEF in the second-order LADRC are reasonable will directly affect the performance of the entire controller. The parameters that need to be set for each part are: observer gains l_1, l_2 and l_3 of the third-order LESO and controller parameters k_p and k_d of the LSEF. It can be individually set every section according to the separation principle [15].

3.4.1. Parameters Tuning of Third-Order LESO

From Equation (12), the characteristic equation of the third-order LESO can be obtained as Equation (17):

$$s^3 + l_1 s^2 + l_2 s + l_3 = 0 \tag{17}$$

According to reference [17], in order to ensure that the system adjustment time is short and the stability is good, the pole of the characteristic equation is arranged at $-\omega_0$ by the pole configuration method. Then Equation (17) is transformed into Equation (18):

$$s^3 + l_1 s^2 + l_2 s + l_3 = (s + \omega_0)^3 = 0 \tag{18}$$

Thus, the observer gains of the third-order LESO is given as Equation (19):

$$\begin{cases} l_1 = 3\omega_0 \\ l_2 = 3\omega_0^2 \\ l_3 = \omega_0^3 \end{cases} \tag{19}$$

where ω_0 is the observer bandwidth. Thus ω_0 is the only parameter to be set in LESO. The larger the ω_0, the wider the bandwidth of LESO, the higher the accuracy of tracking state variables and so

the better the control quality of the controller [27]. However, in the actual parameter setting that the ω_0 too large will also lead to the amplification of measurement noise which is not conducive to the control of the system. Therefore, ω_0 should not be too large in the actual project. The influence of observation noise on the system should be considered comprehensively and the size of parameters should be adjusted appropriately.

3.4.2. Parameters Setting of LSEF

According to Equation (16), the characteristic equation of the closed-loop system is Equation (20):

$$s^2 + k_d s + k_p = 0 \tag{20}$$

Similarly, according to reference [17], the pole of the characteristic equation is placed at $-\omega_c$ in order to ensure the rapid response of the system. Then Equation (20) becomes Equation (21):

$$s^2 + k_d s + k_p = (s + \omega_c)^2 = 0 \tag{21}$$

Therefore, the controller parameters in the LSEF are respectively expressed as Equation (22):

$$\begin{cases} k_p = \omega_c^2 \\ k_d = 2\omega_c \end{cases} \tag{22}$$

where ω_c is the bandwidth of the controller. It can be seen that the only parameter to be set in PD controller is ω_c. The larger the ω_c, the faster the output response of the system and the shorter the dynamic process time. However, in the actual engineering parameter setting process, larger ω_c will increase the burden of PD controller, resulting in increased sensitivity of the system to noise which will lead to system instability in serious cases. Therefore, the parameter tuning of the actual engineering needs to balance the rapidity and stability of the system.

In the process of parameter setting in this paper, ω_c is kept unchanged and ω_0 is gradually increased until the influence of noise meets the requirements of the system. Then gradually increase ω_c, decrease ω_0 when the influence of noise is unbearable and then increase ω_c, so as to achieve the desired control effect. Finally, second-order LADRC parameters of the outer voltage loop were selected as $\omega_c = 6000$ and $\omega_0 = 700$.

4. Frequency Domain Characteristic Analysis of Third-Order LESO

Since the third-order LESO is the core component that affects the performance of the second-order LADRC controller [28,29], thus the classical frequency domain analysis method is used to analyze the convergence of the third-order LESO and the influence of the total disturbance on the performance of the third-order LESO.

4.1. Convergence and Estimation Error Analysis of Third-Order LESO

Converting Equation (12) into the form of transfer function and substitute in the values of Equation (19), then the transfer functions of z_1, z_2 and z_3 can be respectively given as Equations (23)–(25):

$$Z_1(s) = \frac{3\omega_0 s^2 + 3\omega_0^2 s + \omega_0^3}{(s+\omega_0)^3} Y(s) + \frac{b_0 s}{(s+\omega_0)^3} U(s) \tag{23}$$

$$Z_2(s) = \frac{\left(3\omega_0^2 s + \omega_0^3\right)s}{(s+\omega_0)^3} Y(s) + \frac{b_0(s+3\omega_0)s}{(s+\omega_0)^3} U(s) \tag{24}$$

$$Z_3(s) = \frac{\omega_0^3 s^2}{(s+\omega_0)^3} Y(s) - \frac{b_0\omega_0^3}{(s+\omega_0)^3} U(s) \tag{25}$$

The tracking error of each state variable of the observer is defined as $e_1 = z_1 - y$, $e_2 = z_2 - \dot{y}$ and $e_3 = z_3 - f$. So, the transfer function of the tracking error of each state variable can obtained by Equations (26)–(28):

$$E_1(s) = \frac{b_0 s}{(s+\omega_0)^3} U(s) - \frac{s^3}{(s+\omega_0)^3} Y(s) \tag{26}$$

$$E_2(s) = \frac{b_0 s(s+3\omega_0)}{(s+\omega_0)^3} U(s) - \frac{(s+3\omega_0)s^3}{(s+\omega_0)^3} Y(s) \tag{27}$$

$$E_3(s) = b_0 \left(1 - \frac{\omega_0^3}{(s+\omega_0)^3}\right) U(s) - \left(1 - \frac{\omega_0^3}{(s+\omega_0)^3}\right) s^2 Y(s) \tag{28}$$

According to the principle of classical control theory, let $Y(s) = \frac{K}{s}$, $U(s) = \frac{K}{s}$ (K is a constant). Then the steady-state error of each state variable tracking can be given as Equation (29):

$$\begin{cases} e_{1s} = \lim\limits_{s\to 0} s E_1(s) = 0 \\ e_{2s} = \lim\limits_{s\to 0} s E_2(s) = 0 \\ e_{3s} = \lim\limits_{s\to 0} s E_3(s) = 0 \end{cases} \tag{29}$$

It can be seen from the above equation that the third-order LESO has good convergence and can track the various state variables of the system without any difference.

4.2. Analysis of the Influence of Total Disturbance on Third-Order LESO Performance

According to the estimation error of third-order LESO for each state variable of the system defined in Section 4.1, it is Equation (30):

$$\begin{cases} e_1 = z_1 - x_1 = z_1 - y \\ e_2 = z_2 - x_2 \\ e_3 = z_3 - x_3 = z_3 - f \end{cases} \tag{30}$$

The equation of state of third-order LESO estimation error can be obtained by Equation (12) minus Equation (10), giving Equation (31):

$$\begin{cases} \dot{e}_1 = e_2 - 3\omega_0 e_1 \\ \dot{e}_2 = e_3 - 3\omega_0^2 e_1 \\ \dot{e}_3 = -\omega_0^3 e_1 - \dot{f} \end{cases} \tag{31}$$

After the Laplace transform on the above formula, the transfer function of each state estimation error with respect to the total disturbance is obtained as Equation (32):

$$\begin{cases} G_{e_1}(s) = \frac{e_1(s)}{f(s)} = \frac{s}{s^3+3\omega_0 s^2+3\omega_0^2 s+\omega_0^3} \\ G_{e_2}(s) = \frac{e_2(s)}{f(s)} = \frac{s(s+3\omega_0)}{s^3+3\omega_0 s^2+3\omega_0^2 s+\omega_0^3} \\ G_{e_3}(s) = \frac{e_3(s)}{f(s)} = \frac{s(s^2+3\omega_0 s+3\omega_0^2)}{s^3+3\omega_0 s^2+3\omega_0^2 s+\omega_0^3} \end{cases} \tag{32}$$

It can be seen from Equation (32) that the total disturbance is the only factor affecting the estimation error of third-order LESO. Now, the influence of the total disturbance on each estimation error of third-order LESO is analyzed in detail with the help of the Bode diagram in the frequency domain. The frequency domain curve comparing the estimated errors of each state by changing ω_0 are shown in Figure 6.

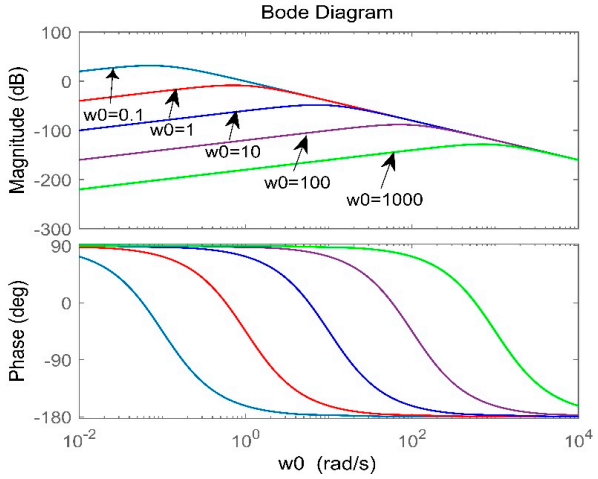

(**a**) $G_{e_1}(s)$ Frequency domain characteristic curve

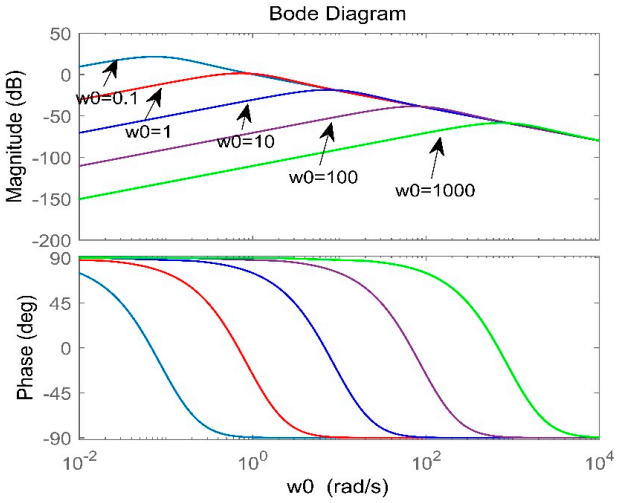

(**b**) $G_{e_2}(s)$ Frequency domain characteristic curve

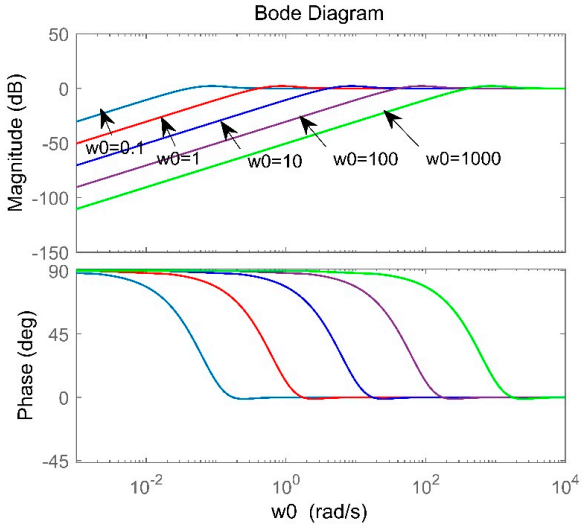

(**c**) $G_{e_3}(s)$ Frequency domain characteristic curve

Figure 6. Frequency domain curve of each state estimation error.

It can be seen from the frequency domain characteristic curve shown in Figure 6 that, firstly, as the observer bandwidth ω_0 increases, the influence of the total disturbance on the state estimation errors of the third-order LESO is gradually reduced. Among them, the estimated error value caused by the total disturbance in the middle and low frequency bands is relatively obvious. However, it has no effect on the estimation error of the high frequency band. Secondly, as the observer bandwidth ω_0 increases, the phase margin of each error transfer function has not changed significantly. The total perturbation signal at the frequency around ω_0 has the greatest influence on the estimation error of each state of the third-order LESO. For the total disturbance with a frequency greater than the observer bandwidth frequency, the third-order LESO cannot accurately estimate it, which results in the estimated performance of the LESO being affected by the bandwidth.

5. Design of Voltage Outer Loop Control System Based on Second-Order LADRC

According to the above analysis, to build the voltage outer loop controller of wind power grid-connected inverter based on second-order LADRC, the most important thing is to build the third-order LESO of the system. The mathematical model of the DC side of grid-connected inverter based on the switch function under the two-phase synchronous rotation dq coordinate system is shown in Equation (33):

$$\frac{dU_{\mathrm{dc}}}{dt} = -\frac{3}{2C}\sum_{k=d,q} S_k i_k + \frac{1}{C} i_{\mathrm{dc}} \tag{33}$$

By differentiating both sides of the above equation we get Equation (34):

$$\frac{d^2U_{\mathrm{dc}}}{dt^2} = \frac{3}{2LC}\sum_{k=d,q}\left(S_k i_k \mathrm{R} - S_k e_k\right) + \frac{3\omega}{2C}\left(S_{\mathrm{q}} i_{\mathrm{d}} - S_{\mathrm{d}} i_{\mathrm{q}}\right) + \frac{3}{2LC}\sum_{k=d,q} S_k U_k \tag{34}$$

The differential equation of Equation (34) can transformed into the state-space form of Equation (35):

$$\begin{cases} \begin{bmatrix} \dot{x}_1 \\ \dot{x}_2 \\ \dot{x}_3 \end{bmatrix} = \begin{bmatrix} 0 & 1 & 0 \\ 0 & 0 & 1 \\ 0 & 0 & 0 \end{bmatrix} \begin{bmatrix} x_1 \\ x_2 \\ x_3 \end{bmatrix} + \begin{bmatrix} 0 & 0 \\ b_0 & 0 \\ 0 & 1 \end{bmatrix} \begin{bmatrix} u \\ h \end{bmatrix} \\ y = x_1 \end{cases} \tag{35}$$

where $b_0 = 3/2LC$. State variables x_1 and x_2 are the output $y = U_{\mathrm{dc}}$ and its differential. $x_3 = f$ is the extended state variable and it is expressed as the total disturbance of the system, whose expression is $f = (3/2LC)\sum_{k=d,q}\left(S_k i_k \mathrm{R} - S_k e_k\right) + (3\omega/2\mathrm{C})\left(S_{\mathrm{q}} i_{\mathrm{d}} - S_{\mathrm{d}} i_{\mathrm{q}}\right)$ and its differential is h.

According to Equations (12) and (19), the third-order LESO of the voltage outer loop can be obtained as Equation (36):

$$\begin{cases} \dot{z}_1 = z_2 - 3\omega_0(z_1 - U_{\mathrm{dc}}) \\ \dot{z}_2 = z_3 - 3\omega_0^2(z_1 - U_{\mathrm{dc}}) + b_0 u \\ \dot{z}_3 = -\omega_0^3(z_1 - U_{\mathrm{dc}}) \end{cases} \tag{36}$$

When the parameter ω_0 is precisely set, the output z_1, z_2 and z_3 of the state observer respectively converge to the DC side bus voltage U_{dc}, the differential signal of U_{dc} and the total disturbance of the system.

LSEF can be designed as Equation (37):

$$\begin{cases} u_0 = \omega_c^2\left(U_{\mathrm{dc}}^* - z_1\right) - 2\omega_{\mathrm{c}} z_2 \\ u = (-z_3 + u_0)/b_0 = i_{\mathrm{d}}^* \end{cases} \tag{37}$$

where U^*_{dc} is the given voltage of the DC bus and i^*_d is the given reference value of the d-axis of the inner loop of the current. The control block diagram of voltage outer loop grid-connected inverter based on second-order LADRC is shown in Figure 7.

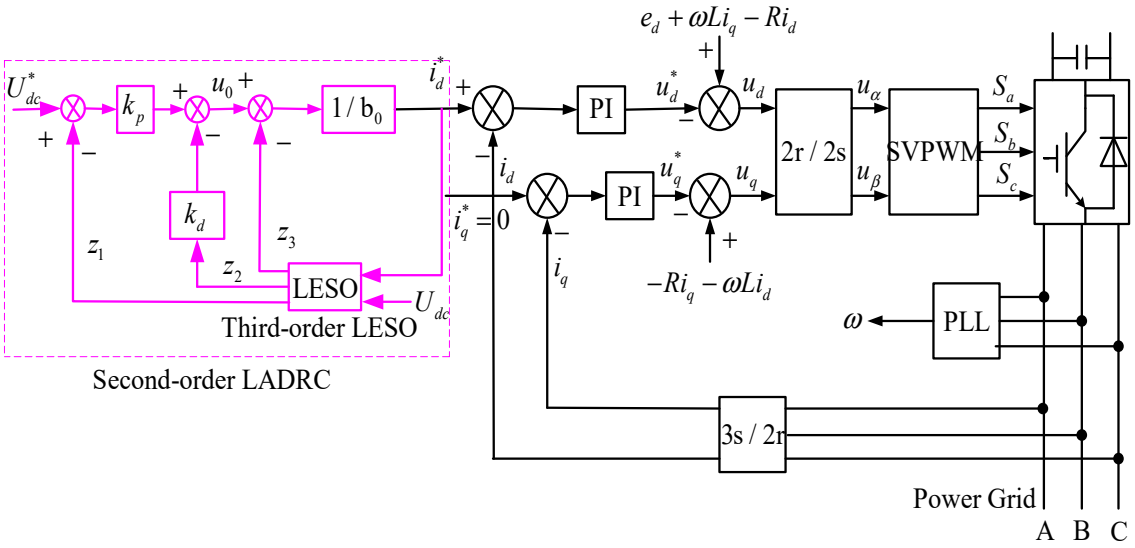

Figure 7. Control block diagram of voltage outer loop grid-connected inverter based on second-order LADRC.

6. Contrastive Simulation Analysis

In order to verify the effectiveness of the control method designed in this paper, the simulation model of a 1.5 MW direct-driven permanent magnet wind power generation system was built in Matlab/Simulink. The main parameters of the system are shown in Table 1 and the controller parameters are shown in Table 2. This contrasts with the traditional control method.

Table 1. Simulation parameters of 1.5 MW direct-drive permanent magnet generator.

Parameter	Parameter Value
Base Power/MW	1.5
Base Voltage/V	690
Dc Bus Voltage/V	1070
Dc Bus Capacitance/μF	240
Grid Side Incoming Line Equivalent Resistance/Ω	0.942
Grid Side LC Filter Capacitance/μF	147
Grid Side LC Filter Inductance/μH	120

Table 2. Controller parameters.

Parameter	Parameter Value
Observer Bandwidth/ω_0	700
Controller Bandwidth/ω_c	6000
Outer Loop PI Controller Parameters/k_{up}	38.4
Outer Loop PI Controller Parameters/k_{ui}	6.144
Inner Loop PI Controller Parameters/k_{ip}	0.2
Inner Loop PI Controller Parameters/k_{ii}	1.57

6.1. Comparative Analysis of Steady-State Control Performance

The system works in the absence of internal and external disturbance. Only the voltage outer loop controller is different and other conditions are the same, and the system simulation time is 3 s. At this time, the simulation waveform of bus voltage on the DC side of the grid-connected inverter in two control modes is shown in Figure 8:

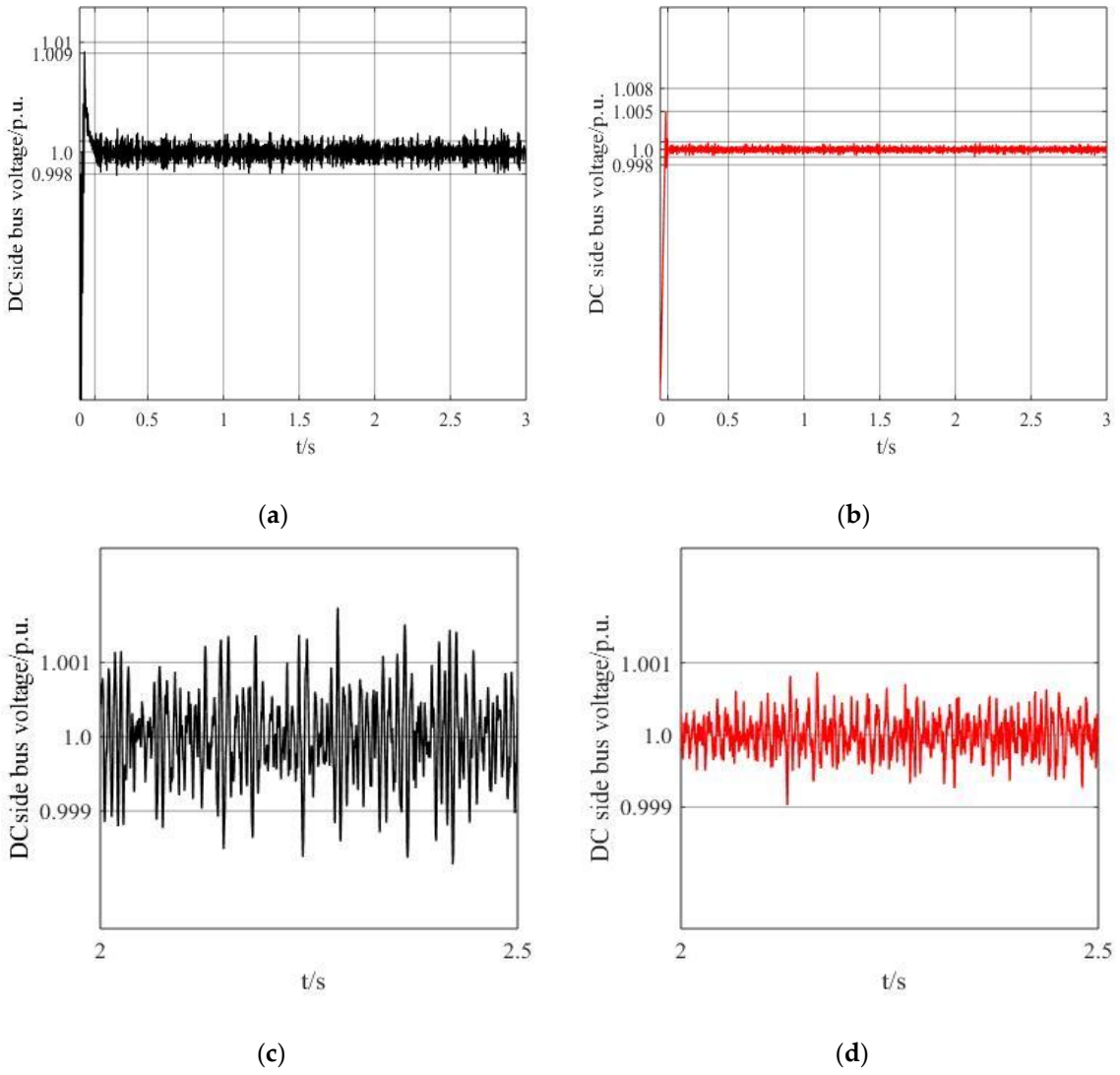

Figure 8. Contrastive of DC side bus voltage waveform under two control modes during steady operation. (**a**) traditional control mode; (**b**) second-order LADRC control mode; (**c**) DC side bus voltage fluctuation range under traditional control mode; (**d**) DC side bus voltage fluctuation range under second-order LADRC control mode.

The DC side bus voltage waveform of the grid-connected inverter maximum value exceeds 1.009 p.u. before entering the stable state under the traditional control mode as shown in Figure 8a. It enters the steady state at about 100 ms, that is, the DC side bus voltage reaches the rated value 1.0 p.u. It can be seen from the partial enlargement diagram of 2–2.5 s in Figure 8c that the fluctuation of the DC side bus voltage is large under the traditional control mode. In Figure 8b, for the DC side bus voltage under the second-order LADRC control mode, the maximum amplitude before entering stability is 1.005 p.u. It is stable at about 50 ms which is faster than the traditional control mode. It can be seen from the partial enlargement diagram of 2–2.5 s in Figure 8d that the fluctuation range of

the DC side bus voltage amplitude is smaller than the traditional control mode and the DC side bus voltage is more stable.

It can be seen from Figure 9 that the harmonic of grid-connected current can be significantly suppressed under the second-order LADRC control mode. The harmonic content of grid-connected current decreased from 2.13% to 1.55% which made the sinusoidal waveform of grid-connected current fuller and improved the grid-connected power quality.

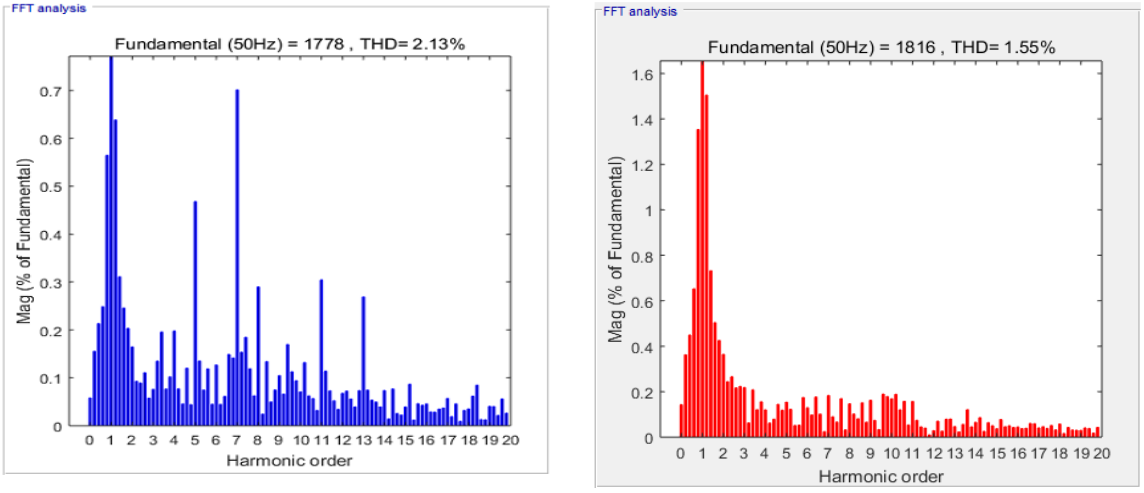

(**a**) (**b**)

Figure 9. Comparison of harmonic content of grid-connected current in two control modes. (**a**) harmonic analysis under traditional control mode; (**b**) harmonic analysis under second-order LADRC control mode.

6.2. Contrastive Analysis of Controller Immunity Characteristics

In order to verify that the voltage outer loop based on second-order LADRC controller designed in this paper has better disturbance rejection characteristics than the traditional PI controller, the dynamic response speed and steady-state performance of the bus voltage on the DC side of the grid-connected inverter under the two control modes were compared with the disturbance of sudden change of motor load, symmetrical rise of power grid voltage and symmetrical drop of power grid voltage during the steady state operation of the system.

6.2.1. Comparison of Two Control Methods When the Grid Voltage Swell Symmetrically

Set the magnitude of symmetrical swell of power grid voltage due to the fault to be 15%, the fault starting time to be 2.1 s, the fault ending time to be 2.4 s and the system simulation time to be 3 s. The other conditions are the same, comparing the waveform of the DC side bus voltage under the two control methods. The voltage waveform of the grid during symmetrical swell is shown in Figure 10a. The DC side bus voltage waveform under two control modes are shown in Figure 10b.

It can be seen from Figure 10b that when the grid voltage swells symmetrically due to the fault, the maximum value of the DC side bus voltage rises to 1.09 p.u. under the traditional control mode and the voltage fluctuation range is 1.044–1.09 p.u. It is stable at 1.057 p.u. after 65 ms. Under the second-order LADRC control mode, the maximum DC bus voltage rise is 1.076 p.u. and the voltage fluctuation range is 1.055–1.076 p.u., whose fluctuation frequency is smaller. It is stable at 1.057 p.u. after 20 ms. At the end of the fault, the maximum value of the DC side bus voltage under the traditional control mode rises to 1.08 p.u. and the voltage fluctuation range is 0.958–1.08 p.u. and finally stabilizes at 1.0 p.u. after 80 ms. Under the second-order LADRC control mode, the DC side bus voltage rises to 1.065 p.u. and the voltage fluctuation range is 0.983–1.065 p.u. whose number of fluctuations is smaller and finally stabilizes at 1.0 p.u. after 25 ms.

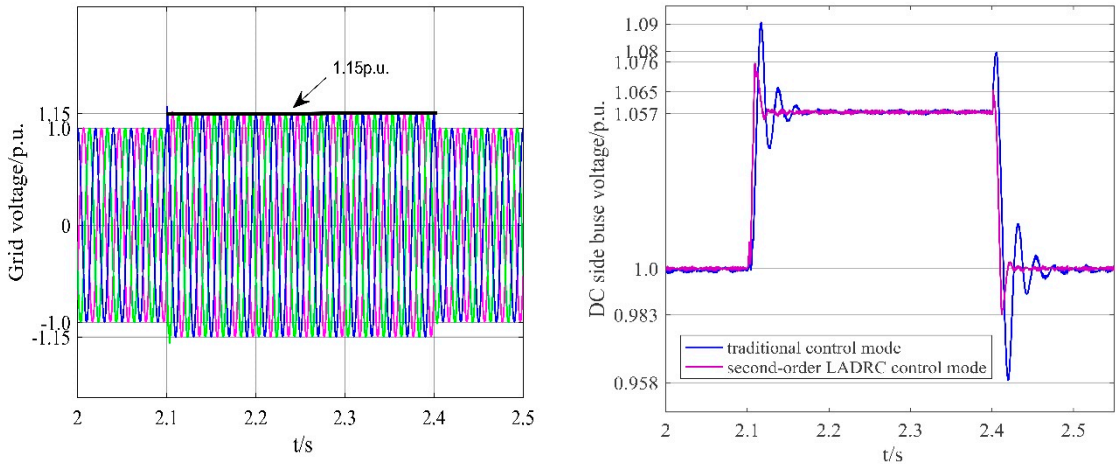

(**a**) (**b**)

Figure 10. DC side bus voltage waveform under two control modes when the grid voltage symmetric swells by 15%. (**a**) grid voltage waveform; (**b**) DC side bus voltage.

6.2.2. Comparison of Two Control Methods When the Grid Voltage is Symmetrically Dropped

Set the magnitude of symmetrical drop of power grid voltage due to fault to be 10%, the fault start time is 2.1s and the fault end time is 2.4s and the system simulation time is 3s. The other conditions are the same, comparing the DC side bus voltage waveform under the two control modes. The grid voltage waveform is shown in Figure 11a and the DC side bus voltage waveform under the two control modes are shown in Figure 11b.

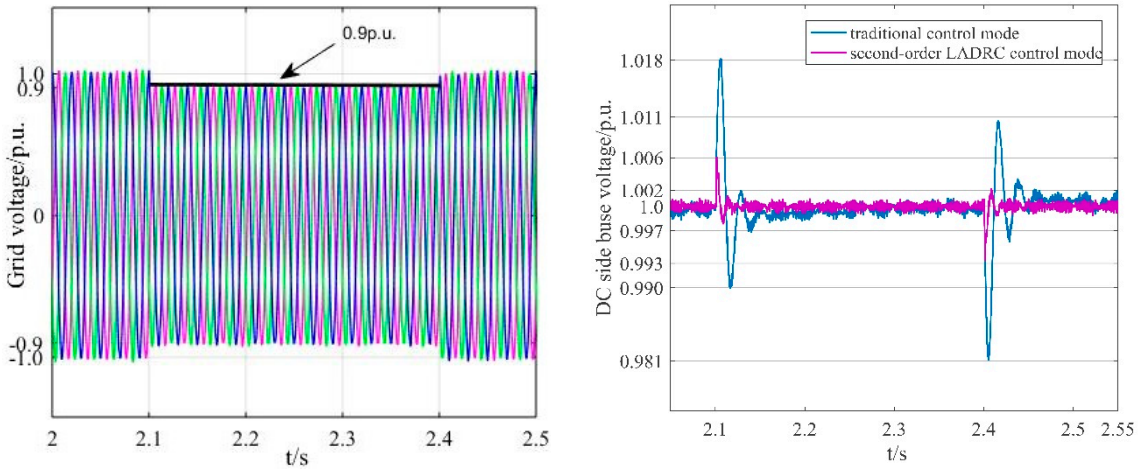

(**a**) (**b**)

Figure 11. DC side bus voltage waveform under two control modes when the grid voltage is symmetrically dropped by 10%. (**a**) grid voltage waveform; (**b**) DC side bus voltage.

It can be seen from Figure 11b that when the grid voltage is symmetrically dropped, the maximum value of the DC side bus voltage is 1.018 p.u. under the traditional control mode at the initial fault time and the voltage fluctuation amplitude is 0.990–1.018 p.u. It is stable at 1.0 p.u. after 100 ms. Under the second-order LADRC control mode, the maximum value of the DC side bus voltage is 1.006 p.u. and the voltage fluctuation range is 0.99–1.006 p.u. which is smaller. It is stable at 1.0 p.u. after 20 ms. At the end of the fault, the DC side bus voltage fluctuation range is 0.981–1.011 p.u. under the traditional control mode and finally reaches the steady state value after 110 ms. Under the second-order LADRC

control mode, the DC side bus voltage fluctuation range is 0.993–1.002 p.u., which is smaller and the transition time is shorter. It enters the steady state value of 1.0 p.u. after 25 ms.

6.2.3. Comparative Analysis of DC Side Bus Voltage under Two Control Modes When the Motor Load Suddenly Changes

During the steady-state operation of the wind power grid-connected inverter system, the load on the motor side suddenly changes at 2.2 s. The comparison waveform of the DC side bus voltage under the two control modes is shown in Figure 12. The system simulation time is 3 s.

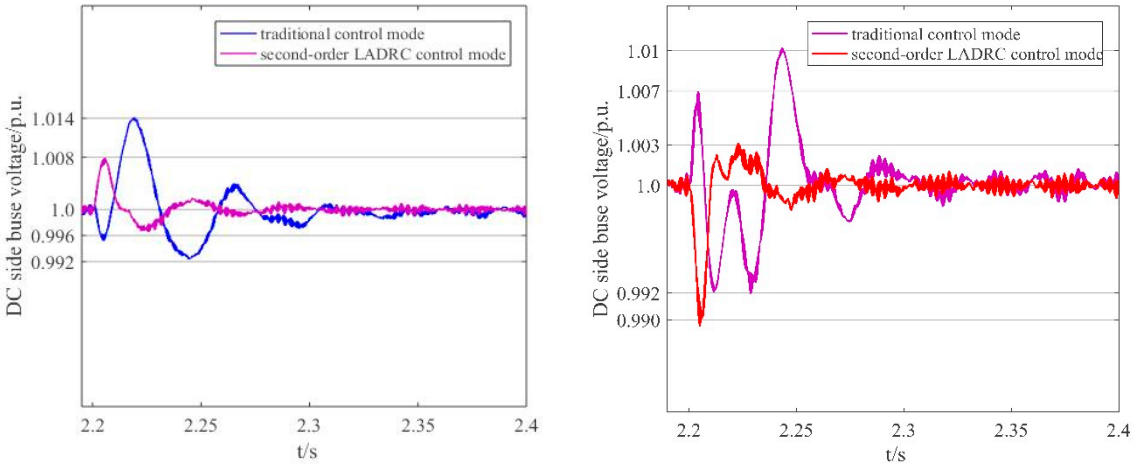

(**a**) (**b**)

Figure 12. DC side bus voltage comparison waveform when the motor load suddenly changes. (**a**) DC side bus voltage comparison waveform when the motor load suddenly increases; (**b**) DC side bus voltage comparison waveform when motor load suddenly decreases.

It can be seen from Figure 12a that when the motor load suddenly increases during the steady-state operation of the system, the fluctuation range of the DC side bus voltage is 0.992–1.014 p.u. under the traditional control mode and the number of fluctuations is more. Finally it enters stable after 135 ms. Under the second-order LADRC control mode, the DC side bus voltage fluctuation range is 0.996–1.008 p.u. whose fluctuation period is short, and it becomes stable after 85 ms. Figure 12b shows that when the motor load suddenly decreases during the steady-state operation of the system, the DC side bus voltage fluctuates under the traditional control mode from 0.992–1.01 p.u., with large fluctuation range and long period. It will enter stability after 120 ms. Under the second-order LADRC control mode, the DC side bus voltage fluctuation range is 0.990–1.003 p.u., the fluctuation period is short, and it is stable after 100 ms.

In summary, comparing the dynamic response speed and steady-state performance of DC-side bus voltage under the two control modes by applying three different disturbance conditions to the wind power grid-connected inverters during steady-state operation, it can see that the control effect of voltage outer loop based on second-order LADRC is obviously better than that of traditional PI controller.

7. Conclusions

The control of the DC side bus voltage of the wind power grid-connected inverter is an important issue in the wind power generation system. The control performance directly determines the grid-connected power quality of the wind power and whether the whole system can operate stably. In this paper, a voltage outer loop controller based on a second-order LADRC is designed for the wind power grid-connected inverter to improve the dynamic response speed and stability of the DC side bus voltage of the wind turbine grid-connected inverter. The main contributions of this work are:

(i) A second-order LADRC grid-connected inverter voltage outer loop controller that does not depend on the system model was designed. The uncertainties and external disturbances of the system model are regarded as the total disturbances, and the total disturbances are set as the extended state variables of the system. The third-order LESO is used to estimate and track the changes of the system state in real time, thus improving the precise control of the DC side bus voltage.

(ii) The convergence of the third-order LESO in the designed controller and the influence of the total disturbance on its performance were analyzed in detail by using the classical frequency domain analysis method.

(iii) A 1.5 MW direct-driven permanent magnet wind power generation system was built in Matlab/Simlink platform. Compared with the traditional PI control effect, it shows that the second-order LADRC is more capable of treating various disturbances in the system than the PI controller and the controller has strong robustness.

In brief, the control method of the wind power grid-connected inverter based on the second-order LADRC voltage outer loop controller can effectively improve the dynamic response speed and steady-state performance of the DC side bus voltage. Moreover, the voltage fluctuation amplitude of the bus on the DC side can be well suppressed under various disturbances. It can provide effective reference and help for improving the quality of grid-connected power for wind power generation in complex situations.

Author Contributions: Y.M. conceived the main idea for the second-order LADRC and performed the overall analysis; F.Z. and X.Z. wrote this paper; M.L. and B.Y. contributed to analyzing the experimental results.

Funding: This work was funded by National Natural Science foundation of China (NO. 51877152) and Natural Science Foundation of Tianjin of China (No. 18JCZDJC97300).

Acknowledgments: The authors are thankful to National Natural Science foundation of China (No. 51877152), Natural Science Foundation of Tianjin of China (No. 18JCZDJC97300) and Tianjin University of Technology for their support.

Conflicts of Interest: The authors declare no conflict of interest.

References

1. Soliman, M.A.; Hasanien, H.M.; Azazi, H.Z.; El-Kholy, E.E. An Adaptive Fuzzy Logic Control Strategy for Performance Enhancement of a Grid-Connected PMSG-Based Wind Turbine. *IEEE Trans. Ind. Inf.* **2019**, *15*, 3163–3173. [CrossRef]
2. Liao, C.Y.; Lin, W.S.; Chen, Y.M.; Chou, C.Y. A PV Micro-inverter with PV current decoupling strategy. Title of the article. *IEEE Trans. Power Electron.* **2017**, *32*, 6544–6557. [CrossRef]
3. Manoj, S.P.; Vijayakumari, A.; Sasi, K.K. Development of a Comprehensive MPPT for grid-connected wind turbine driven PMSG. *Wind Energy* **2019**, *22*, 732–744.
4. Lee, S.W.; Chun, K.H. Adaptive Sliding Mode Control for PMSG Wind Turbine Systems. *Energies* **2019**, *12*, 595. [CrossRef]
5. Liu, X.R.; Gao, C.; Wang, Z.L. A Nonlinear Disturbance Observer Based DC-bus Voltage Control for PV Grid-connected Inverter. *Power Syst. Tech.* **2019**, *5*, 1–11. Available online: https://kns.cnki.net/KCMS/detail/11.2410.TM.20190521.1646.001.html?uid=WEEvREcwSlJHSldRa1FhdXNXaEhoOG5DWWlTRVhmWEVmY1lPckdiTThjOD0=$9A4hF_YAuvQ5obgVAqNKPCYcEjKensW4IQMovwHtwkF4VYPoHbKxJw!!&v=MDc2NzBEa1dydkxJRjg9SVRyQmZiRzRIOWpNcW8xRVpPc0xZdzlNem1SbjZqNTdUM2ZscVdNMENMTDdSN3FlYnVkdUZp (accessed on 15 September 2019).
6. Muslem, U.; Saad, M.; Marco, R. High Performance Modified Model Predictive Control of a Voltage Source Inverter. *Electr. Power Compon. Syst.* **2018**, *46*, 600–613.
7. Youssef, E.; Mohammed, O.; Mohamed, M. A performance comparison of a nonlinear and a linear control for grid connected PMSG wind energy conversion system. *Int. J. Electr. Power Energy Syst.* **2015**, *68*, 180–194.
8. Hossain, M.A.; Pota, H.R.; Haruni, A.M.O.; Hossain, M.J. DC-link voltage regulation of inverters to enhance microgrid stability during network contingencies. *Electr. Power Syst. Res.* **2017**, *147*, 233–244. [CrossRef]
9. Yan, J.H.; Lin, H.Y.; Feng, Y.; Zhu, Z.Q. Control of a grid-connected direct-drive wind energy conversion system. *Renew. Energy* **2014**, *66*, 371–380. [CrossRef]

10. Han, J.Q. *Active Disturbance Rejection Control Technique-The Technique for Estimating and Compensating the Uncertainties*; National Defense Industry Press: Beijing, China, 2008.
11. Han, J.Q. From PID to active disturbance rejection control. *IEEE Trans. Ind. Electron.* **2009**, *56*, 900–906. [CrossRef]
12. Yang, C.X.; Yang, X.; Yuri, A.W.S. An ADRC-Based Control Strategy for FRT Improvement of Wind Power Generation with a Doubly-Fed Induction Generator. *Energies* **2018**, *11*, 1150. [CrossRef]
13. Coral, E.H.; Cortés, R.J.; Dorado, R. Rejection of varying-frequency periodic load disturbances in wind-turbines through active disturbance rejection-based control. *Renew. Energy* **2019**, *141*, 217–235. [CrossRef]
14. Saleem, M.; Choi, K.Y.; Kim, R.Y. Resonance damping for an LCL filter type grid-connected inverter with active disturbance rejection control under grid impedance uncertainty. *Int. J. Electr. Power Energy Syst.* **2019**, *109*, 444–454. [CrossRef]
15. Xu, X.N.; Zhou, X.S.; Ma, Y.J.; Gao, Z.Q. Micro Grid Operation Controller Based on ADRC. *High Volt. Eng.* **2016**, *42*, 3336–3346.
16. Gao, Z. Active disturbance rejection control: A paradigm shift in feedback control system design. In Proceedings of the 2006 American Control Conference, Minneapolis, MN, USA, 14–16 June 2006; p. 7.
17. Gao, Z. Scaling and bandwidth-parameterization based controller tuning. In Proceedings of the 2003 American Control Conference, Denver, CO, USA, 4–6 June 2003; pp. 4989–4996.
18. Su, Z.Q.; Zhou, M.; Han, F.F.; Zhu, Y.W.; Song, D.L.; Guo, T.T. Attitude control of underwater glider combined reinforcement learning with active disturbance rejection control. *J. Mar. Sci. Technol.* **2019**, *24*, 686–704. [CrossRef]
19. Zhao, L.; Dai, L.; Xia, Y.; Li, P. Attitude control for quadrotors subjected to wind disturbances via active disturbance rejection control and integral sliding mode control. *Mech. Syst. Signal Process.* **2019**, *129*, 531–545. [CrossRef]
20. Wu, Y.; Wang, L.; Zhang, J.; Li, F. Path Following Control of Autonomous Ground Vehicle Based on Nonsingular Terminal Sliding mode and Active Disturbance Rejection Control. *IEEE Trans. Veh. Technol.* **2019**, *7*, 6379–6390. [CrossRef]
21. Yuan, Y.; Wang, Z.; Yu, Y.; Guo, L.; Yang, H. Active disturbance rejection control for a pneumatic motion platform subject to actuator saturation: An extended state observer approach. *Automatica* **2019**, *107*, 353–361. [CrossRef]
22. Lind, P.G.; VeraTudela, L.; Wächter, M.; Kühn, M.; Peinke, J. Normal behaviour models for wind turbine ibrations: Comparison of neural networks and a stochastic approach. *Energies* **2017**, *10*, 1944. [CrossRef]
23. Yanghong, T.; Haixia, Z.; Ye, Z. A Simple-to-Implement Fault Diagnosis Method for Open Switch Fault in ind System PMSG Drives without Threshold Setting. *Energies.* **2018**, *11*, 2571. [CrossRef]
24. Song, Z.; Tian, Y.; Yan, Z.; Chen, Z. Direct power control for three-phase two-level voltage source rectifiers based on extended-state observation. *IEEE Trans. Ind. Electron.* **2016**, *63*, 4593–4603. [CrossRef]
25. Malinowski, M.; Jasinski, M.; Kazmierkowski, M.P. Simple direct power control of three-pase PWM rectifier using space-vector modulation (DPC-SVM). *IEEE Trans. Ind. Electron.* **2004**, *51*, 447–454. [CrossRef]
26. Pu, Z.Q.; Yuan, R.Y.; Yi, J.Q.; Tan, X.M. A class of adaptive extended state observers for nonlinear disturbed systems. *IEEE Trans. Ind. Electron.* **2015**, *62*, 5858–5869. [CrossRef]
27. Gao, Z.; Huang, Y.; Han, J. An alternative paradigm for control system design. In Proceedings of the 40th IEEE Conference on Decision and Control, Orlando, FL, USA, 4–7 December 2001.
28. Herbst, G. A simulative study on Active Disturbance Rejection Control (ADRC) as a control tool for ractitioners. *Electronics* **2013**, *2*, 246–279. [CrossRef]
29. He, T.; Wu, Z.; Shi, R.; Li, D.; Sun, L.; Wang, L.; Zheng, S. Maximum sensitivity-constrained data-driven ctive disturbance rejection control with application to airflow control in power plant. *Energies* **2019**, *12*, 231. [CrossRef]